IEEE Access
Multidisciplinary | Rapid Review | Open Access Journal

Received 24 January 2025, accepted 9 February 2025, date of publication 13 February 2025, date of current version 20 February 2025.

*Digital Object Identifier 10.1109/ACCESS.2025.3541352*

RESEARCH ARTICLE

# City-Scale Spatio-Temporal Modeling of 5G Downlink Exposure of Users and Non-Users by Ray-Tracing in a Real Urban Environment

**MATTHIAS LEEMAN, ROBIN WYDAEGHE, JEROEN VAN DER STRAETEN, SAMUEL GOEGEBEUR, GÜNTER VERMEEREN, AND WOUT JOSEPH, (Senior Member, IEEE)**
Department of Information Technology, Ghent University, 9052 Ghent, Belgium
imec, 9052 Ghent, Belgium

Corresponding author: Matthias Leeman (Matthias.Leeman@UGent.be)

This work was supported by the 5G expOsure, causaL effects and rIsk perception through citizen engAgemenT (GOLIAT) Project through European Union's Horizon Europe Research and Innovation Program under Grant 101057262.

**ABSTRACT** In 5G networks, base stations dynamically form directional beams toward users, coupling the spatial and temporal variations of electromagnetic field exposure. This interdependence introduces significant challenges to exposure modelling, as spatial and temporal components are often evaluated separately. Therefore, we propose a novel spatio-temporal method that incorporates both active users and non-users in realistic 5G exposure simulations. Pedestrian movement is modelled using an agent-based model, and ray-tracing techniques are employed to simulate electric field strengths. Unlike prior studies that focus mainly on static scenarios, or dynamic settings without accounting for precoding effects, our work integrates precoding techniques with dynamic users. In addition, this work also provides a comprehensive comparison of exposure levels for users and non-users. The proposed method is validated with increasing complexity: single-user, two-user, and multi-user scenarios (10 to 50 users). In addition, different precoding techniques and antenna configurations are investigated. The results show that users experience 5.2 dB to 3.7 dB higher field strengths for $8 \times 8$ antenna arrays compared to $4 \times 4$ arrays, highlighting the increased directionality of larger arrays. Non-users also experience increased exposure, with median differences up to 2.4 dB. Zero-forcing precoding reduces median exposure for users by up to 9.6 dB and for non-users by 1.1 dB compared to maximum ratio transmission precoding in multi-user settings. Importantly, all exposure levels remain well below 4 % of the ICNIRP guidelines, even under maximum antenna power. These findings provide critical insights into the interaction between antenna configuration, precoding, and user dynamics, offering a novel perspective on exposure modelling in realistic 5G environments.

**INDEX TERMS** 5G, agent-based model, exposure, massive MIMO, precoding, ray-tracing, spatio-temporal.

## I. INTRODUCTION

The fifth generation (5G) of cellular networks is becoming ubiquitous in daily life [1]. To increase spectral efficiency, 5G introduces beamforming as a core technology [2]. This is enabled by Massive Multiple-Input Multiple-Output (MaMIMO) base stations (BSs) directing electromagnetic energy towards active users [3]. To increase data rates, the operating frequency is increased from 4G's typical range of 0.7 GHz to 2.6 GHz to 3.5 GHz or 28 GHz to explore unlicensed GHz-sized bandwidths.

The International Commission on Non-Ionizing Radiation Protection (ICNIRP) provides guidelines on absorption limits of electromagnetic fields (EMFs) in human tissues and in free space [4]. These guidelines specify two key criteria for assessing EMF exposure: *basic restrictions* and *reference levels*. Basic restrictions account for accute health effects of EMF exposure and define the maximum permissible levels of specific energy absorption rate (SAR) and absorbed power density in human tissues for frequencies below 6 GHz. SAR

The associate editor coordinating the review of this manuscript and approving it for publication was Miguel López-Benítez.

reflects the rate at which electromagnetic energy is absorbed by the body and is directly linked to a potential increase in temperature. Whole-body SAR is used to assess general thermal effects across the entire body, while localized SAR focuses on specific regions to address concentrated heating in smaller areas of tissue.

Reference levels, on the other hand, are measurable quantities outside the body, such as electric field strength (E), magnetic field strength (H), and incident power density (S). They serve as practical benchmarks to assess compliance with the basic restrictions. Exceeding these levels necessitates a more detailed evaluation against the basic restrictions to ensure safety. Due to their ease of in-situ measurement, reference levels form the foundation for evaluating exposure levels in experimental and computational studies. These measurable thresholds enable researchers to quantify exposure and address the growing public concerns regarding EMF exposure.

Currently, research on human exposure to EMFs mainly consists of constructing spatial and temporal models in different micro-environments [5]. However, because of the dynamic nature of user movement and active beamforming over time, the spatial distribution of EMFs changes over time [6]. In addition, the number of users also changes throughout the day and throughout the year, introducing a macro-temporal component in exposure assessment [7]. Consequently, a complete assessment of human exposure in 5G networks necessitates a combined analysis of spatial and temporal variations in EMF distributions. This highlights the need for a coupled spatio-temporal model based on a deterministic framework, given the significant influence of environmental features on exposure outcomes.

Simulation models have become increasingly more popular in EMF exposure research, complementing measurement campaigns by providing scalable and flexible tools to analyze complex scenarios. Among these simulation tools, ray-tracing (RT) is widely used due to its accuracy in predicting electromagnetic wave propagation [8]. For example, RT simulations are used to evaluate MaMIMO network performance with precoding in [9], where user placements are randomised within static urban environments. However, such studies are limited to stationary scenarios and do not account for dynamic user mobility. To investigate the interaction of EMFs with the human body, hybrid methods that combine RT with finite-difference time-domain (FDTD) simulations are being explored. In [6], FDTD is integrated into RT simulations to evaluate human exposure, showcasing advanced applications in network planning. Similarly, hybrid RT-FDTD techniques examine human exposure under line-of-sight (LOS) and non-line-of-sight (NLOS) conditions in indoor industrial environments [10]. While these approaches effectively incorporate body effects and enhance exposure assessments, they are constrained in scale and do not address dynamic, city-wide scenarios.

Other studies investigate MaMIMO systems through RT simulations. For instance, [11] analyzes spatial correlation characteristics in controlled indoor environments, while [12] explores spatio-temporal properties, including time-averaged gains under various precoding schemes. Although these studies contribute valuable insights into MaMIMO characteristics, they provide limited understanding of real-world outdoor exposure scenarios, often focusing on single base station (BS) setups with static users. Similarly, [13] uses RT simulations to study multi-user MIMO beamforming, but it lacks the dynamic, city-scale perspective required for broader applicability. The influence of user density in 5G networks is evaluated with RT in [14], where a specific tram car is simulated. While this study does incorporate beamforming effects, it is limited to indoor vehicular environments and does not address broader urban-scale exposure modelling.

Recent advancements in exposure mapping, such as those in [15] and [16], employ static setups and machine learning techniques to enhance modelling accuracy. Despite these efforts, they lack dynamics and fail to capture the complexities of large-scale urban environments comprehensively. These limitations highlight the need for a robust, city-wide simulation framework that integrates dynamic mobility and environmental characteristics to provide a realistic exposure assessment.

Building on this existing work, our paper offers several important contributions to improve the understanding of 5G EMF exposure on a city-wide scale. These contributions address gaps in earlier studies and provide new insights into characteristics of 5G exposure. The key contributions of this work are as follows:

(i) **Introduction of an agent-based model (ABM) for exposure simulations:** We use an ABM to model the behaviour of users and non-users in a realistic city-wide environment. This approach allows us to compare exposure in different real-world scenarios with dynamic movement. Unlike previous studies that often relied on fixed user positions or small areas, our ABM captures the influence of people moving through urban spaces on exposure levels.

(ii) **Use of MRT and ZF precoding in large-scale dynamic simulations:** For the first time, maximum ratio transmission (MRT) and zero-forcing (ZF) precoding are applied to city-scale simulations that include dynamic user movement. Previous works, mainly studied precoding in smaller or static settings. Our study extends these findings by showing how the number of users and their movement patterns affect exposure levels in urban areas.

(iii) **A framework for city-wide exposure mapping:** The hybrid ABM-RT method combines user movement, advanced precoding, and flexible antenna setups to create a robust framework for city-wide exposure mapping based on stochastic results. Unlike earlier methods, which focused on isolated aspects, our framework offers a more complete view of how different factors interact to influence exposure.

This work advances exposure research by integrating dynamic user behaviour, and spatio-temporal variations on

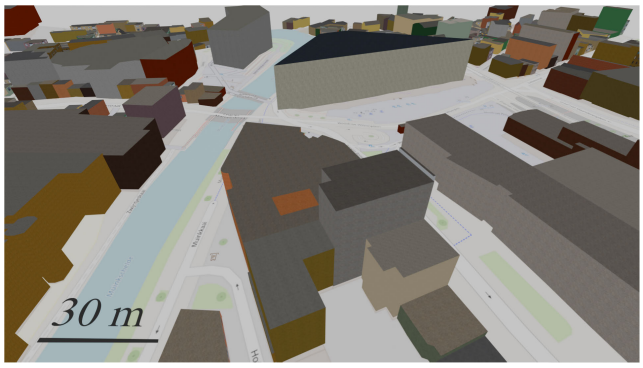


**FIGURE 1.** Birds-eye view of a 3D environment in Ghent, Belgium. The buildings are represented by prismatic shapes on top of the terrain.

a city-wide scale. The framework can also be adapted for other technologies or urban scenarios, making it a valuable tool for network planning and exposure studies. It supports researchers and policymakers by providing detailed data to assess 5G deployment strategies and ensure safer and more efficient urban networks.

## II. METHODS

### A. CONFIGURATION

The terrain data for the simulations is sourced from the USGS SRTM 1 Arc-Second Global dataset [17]. Concrete is used as a default material for the terrain [18]. Building geometries and materials are sourced from OpenStreetMap (OSM) [19]. In the investigated areas, buildings are represented by prismatic shapes placed on top of the terrain [20]. Consequently, finer details of buildings such as roof shapes and facades are not captured. An example of an environment in Ghent, Belgium is shown in Fig. 1. The wavelength is 8 cm at the considered frequency of 3.775 GHz. Therefore, the lack of detail in the OSM dataset cannot only lead to an inaccurate representation of diffuse scattering, but also an underestimation of the channel diversity. This results in less accurate predictions of the exposure levels.

Electrical material parameters are assigned based on the recommendations from the International Telecommunication Union Radiocommunication Sector (ITU-R) [21]. For concrete, the conductivity is $0.096\,\mathrm{S\,m^{-1}}$ and the relative permittivity is 5.310 at a frequency of 3.775 GHz. A single material is assigned to the buildings. As discussed in [22], the accuracy of the RT simulations is highly dependent on the material properties. Therefore, the use of a single material for all buildings may also lead to inaccuracies in the results.

In Belgium, BS information is publicly provided by the government in certificates of conformity [23]. This information includes position, angle, height, total antenna power, frequency, and half-power-beamwidth. To identify relevant BSs for the investigated area, a filtering process is applied based on their positions. Concretely, BSs located within a bounding box 10 % larger than the investigated area are considered, as they may still serve users within the area. A 5G antenna array is generated based on the TR 38.901 specification by the 3rd Generation Partnership Project (3GPP) [24]. Both $4 \times 4$ and $8 \times 8$ antenna arrays are investigated. Cross-polarized elements are used with half-wavelength spacing. Finally, the exposure for both users and non-users is evaluated using an isotropic receiver (Rx) antenna positioned 1.5 m above the ground.

### B. AGENT-BASED MODEL

The movement of people in an urban area is a complex phenomenon [25]. Therefore, an ABM is used to simulate the movement of people. The agents represent pedestrians walking in the environment. These agents include both *users*, that actively engage with the 5G network, and *non-users*. Several assumptions are made in this model:

- All agents are pedestrians.
- The agents move from building to building (starting point and destination outside a building).
- The agents move with a constant speed of 5 km/h.
- The agents do not deviate from the optimal path between starting point and destination, generated by the Google Maps API.
- When the agents reach their destination within the simulated time interval, they return to their respective starting points. For the duration of the simulation, the agents will go back-and-forth from starting point to their destination point.

Population data (with $100\,\mathrm{m} \times 100\,\mathrm{m}$ accuracy) and built-up surface data (with $10\,\mathrm{m} \times 10\,\mathrm{m}$ accuracy) are provided by the Global Human Settlement Layer from the Joint Research Centre of the European Commission [26]. The population data is super-resolved over the built-up surface data to retrieve a $10\,\mathrm{m} \times 10\,\mathrm{m}$ accurate population density. For each agent, a starting point and destination is generated based on this population density. By using the built-up surface data, the assumption is made that each agent moves from building to building. It is important to note that the agents do not enter the buildings, since the focus is on outdoor exposure. The Google Maps API generates walking paths from the starting points to the destinations for each agent [27]. The discrete latitude and longitude coordinates of the walking paths are determined based on the desired time step and the movement speed of the agent ($5\,\mathrm{km\,h^{-1}}$) [25].

The agents are randomly assigned as either users or non-users at the start of the simulation. Once assigned, users and non-users maintain their respective roles throughout the entire simulation duration. The exposure is highly dependant on the specific agent paths within a scenario. Therefore, multiple distinct sets of agent trajectories are generated. This way, a more comprehensive stochastic analysis is achieved based on the probabilistic behaviours (based on population density) of users and non-users. This approach ensures that the results are not dependent on a single set of agent paths but represent the average exposure across multiple possible scenarios.

The assumptions underlying this ABM simplify the representation of human movement and network behaviour. Specifically, the stationary assignment of agents as users or non-users throughout the simulation period does not fully reflect the dynamic nature of network connections and human mobility over time. Additionally, the model assumes that agents follow optimal walking paths and maintain a constant speed, which omits factors such as variations in walking behaviour or spontaneous deviations. Despite these simplifications, the primary focus of this work is on deriving stochastic results that capture the influence of user count, precoding schemes, and antenna configurations on exposure levels. The model is therefore considered sufficient for providing a general understanding of these factors, even if it does not fully account for individual behaviours or connection dynamics.

### C. MODELING

A RT channel model was added to the MATLAB communication toolbox [28]. It is a ray-tracer based on the shooting and bounding rays method (SBR). The RT configuration parameters are provided in Table 1. Since large-scale scenarios are simulated, the simulations are performed on the high-performance computing (HPC) infrastructure provided by Ghent University.

For each time step, the analysis consists of two steps. First, all potential serving antennas are determined for each user. The potential antennas are located within a 1 km radius of the user. The maximum azimuthal angle between the antenna and the user is 90°, ensuring that the antenna exclusively serves users within its forward-facing coverage area. RT is performed between these potential serving antennas and their corresponding users. The output of the ray-tracer includes the pathloss (PL) in dB, angle-of-departure (AoD) and phase shift ($\Delta\phi$) of each ray. In RT simulations, the channel impulse response (CIR) is usually computed as an output [29]. The CIR captures how multipath components arrive with different delays and attenuations. However, since we want to perform precoding, the channel matrix in the frequency domain is computed instead. A channel vector $h_r \in \mathbb{C}^{N\times 1}$ for antenna $i$ can be computed from the output of each ray $r$ as follows:

$$\mathbf{h}_{i,r} = 10^{-\frac{\mathrm{PL}}{20}} e^{j\Delta\phi} \mathbf{a}_i(\theta,\varphi)\,, \tag{1}$$

with

$$\mathbf{a}_i(\theta,\varphi) = \begin{bmatrix} e^{j\mathbf{k}(\theta,\varphi)\cdot\mathbf{r}_1} \\ e^{j\mathbf{k}(\theta,\varphi)\cdot\mathbf{r}_2} \\ \vdots \\ e^{j\mathbf{k}(\theta,\varphi)\cdot\mathbf{r}_N} \end{bmatrix}, \tag{2}$$

the steering vector in the AoD. $\mathbf{r}_n$ is the position vector of the $n$-th element of the array with $N$ elements. $\theta$ and $\varphi$ denote the polar and azimuthal angle in the local coordinate system of the array, such that the wave vector $\mathbf{k}(\theta,\varphi)$ is given by

$$\mathbf{k}(\theta,\varphi) = \frac{2\pi}{\lambda}\left[\sin(\theta)\cos(\varphi),\ \sin(\theta)\sin(\varphi),\ \cos(\theta)\right], \tag{3}$$

**TABLE 1. Propagation model parameters based on literature [30] and standard options provided by MATLAB. The maximum relative path loss is used to determine if a path should be discarded, based on a threshold relative to the strongest ray.**

| | |
|---|---|
| Maximum number of reflections | 5 |
| Maximum number of diffractions | 1 |
| Number of transmissions | 0 |
| Angular separation | 0.25° |
| Maximum relative path loss | 40 dB |

with $\lambda$ the wavelength of the ray.

Let $R(i,k)$ be the set of rays $r$ launched by antenna $i$ received by user $k$. The total channel vector $h_k$ corresponding to user $k$ is found by summing (1) over all rays:

$$\mathbf{h}_{i,k} = \sum_{r\in R(i,k)} \mathbf{h}_{i,r}\,. \tag{4}$$

The corresponding serving antenna for user $k$ is the antenna with the highest channel gain $||h_{i,k}||^2$. The channel vector is added to the channel matrix of the serving antenna. For each antenna that has a served user, the resulting channel matrix $H_i \in \mathbb{C}^{N\times K}$ represents the signal propagation between the BS antenna $i$ and its $K$ served users.

The precoding matrix is defined as:

$$\mathbf{W}_i = \begin{cases} \mathbf{H}_i^H & \text{for MRT} \\ \mathbf{H}_i^H(\mathbf{H}_i\mathbf{H}_i^H)^{-1} & \text{for ZF,} \end{cases} \tag{5}$$

with $(\cdot)^H$ the Hermitian transpose. MRT precoding maximizes the total Signal to Noise Ratio (SNR) of all user. In contrast, ZF precoding maximizes the Signal to Interference plus Noise Ratio (SINR). In this work, MRT precoding is used, unless otherwise specified. The resulting precoding matrix is normalized to satisfy power constraints using vector normalization [31]:

$$\mathbf{W}_i = \sqrt{\frac{P}{K}}\left[\frac{\mathbf{w}_{i,1}}{||\mathbf{w}_{i,1}||}, \frac{\mathbf{w}_{i,2}}{||\mathbf{w}_{i,2}||}, \ldots, \frac{\mathbf{w}_{i,k}}{||\mathbf{w}_{i,k}||}\right], \tag{6}$$

with P the total transmit power of the antenna as specified in the certificate of conformity. This normalization ensures that the maximum antenna power of each transmitting antenna is not exceeded. It also ensures that each user is allocated the same amount of power. The resulting transmit vector $\mathbf{t}_i \in \mathbb{C}^{N\times 1}$ is

$$\mathbf{t}_i = \mathbf{W}_i\mathbf{s}_i\,, \tag{7}$$

with $\mathbf{s}_i$ the symbol vector with symbol 1 for all K users served by antenna $i$. Since the precoding matrix is already normalized, the received signal for user $k$ served by antenna $i$ is

$$y_k = \mathbf{h}_k^T\mathbf{t}_i + z_k\,, \tag{8}$$

$$= \mathbf{h}_k^T\mathbf{w}_k s_k + \sum_{l\neq k}^{K} \mathbf{h}_k^T\mathbf{w}_l s_l + z_k\,, \tag{9}$$

where $z_k$ is a noise term [32]. The total received power for user $k$ by antenna $i$ is then derived from (8):

$$P_r = |\mathbf{h}_k^T \mathbf{t}_i|^2 \,. \tag{10}$$

The SNR and SINR can be derived from (9):

$$\text{SNR} = \frac{|\mathbf{h}_k^T \mathbf{w}_i|^2}{|z_k|^2} \,, \tag{11}$$

$$\text{SINR} = \frac{|\mathbf{h}_k^T \mathbf{w}_i|^2}{\sum_{l \neq k}^{K} |\mathbf{h}_k^T \mathbf{w}_l|^2 + |z_k|^2} \,. \tag{12}$$

For the noise power $|z_k|^2$, an arbitrary thermal noise power is chosen, similarly as in [33]. With a spectral density $N_0 = 5.06 \times 10^{-21}\,\text{W Hz}^{-1}$ and a bandwidth of $B = 100\,\text{MHz}$, the thermal noise power is $|z_k|^2 = N_0 B = 5.06 \times 10^{-13}\,\text{W}$.

In the second step, RT is performed between the transmitting antennas and the non-users. For each agent, both users and non-users, the electric field phasor contributions from all rays from the different transmitting antennas are combined. The received power density $S$ is given by

$$S = \frac{4\pi P_r}{\lambda^2 G} \,, \tag{13}$$

with $G$ the receiver antenna gain and $P_r$ the total received power at the receiver. The electric field strength $E$ is related to $S$ by

$$E = \sqrt{S Z_0} \,, \tag{14}$$

with $Z_0$ the free-space impedance [34]. Therefore, since an isotropic antenna is assumed for the receiver ($G = 1$), the total electric field strength is given by

$$E = \sum_{i}^{N_{\text{Tx}}} \sum_{r \in R(i,k)} \sqrt{\frac{8\pi Z_0}{\lambda^2}} \mathbf{h}_{i,r}^T \mathbf{t}_i \,, \tag{15}$$

where $N_{\text{Tx}}$ is the number of transmitting antennas. The extra factor $\sqrt{2}$ is a result of $E_{\text{peak}} = \sqrt{2} E_{\text{RMS}}$.

The total incident power density can ultimately be compared to the reference value for incident power density at 3.7 GHz defined by the International Commission of Non-Ionizing Radiation Protection (ICNIRP) $S_{\text{limit}} = 10\,\text{W m}^{-2}$ [4]. This comparison is done by considering the ratio $\xi$ between them:

$$\xi = \frac{S}{S_{\text{limit}}} \,, \tag{16}$$

where $S$ is calculated using (14).

### D. SCENARIOS

The ABM-RT method is evaluated in scenarios with increasing complexity. The scenario environments are all located in Ghent, Belgium. The scenarios are classified in three categories, depending on the goal of the analysis and the complexity. A summary of the investigated scenarios is listed in Table 2.

First, a single user path is evaluated with five static non-users (*single user* scenario in Table 2). The walked path is shown in Fig. 2 (user 1). The user is served by one BS site with three antennas, each covering an section of 120° around the site. This simulation is performed with different antenna configurations for the BS. Results obtained using $4 \times 4$ and $8 \times 8$ antenna arrays are compared with results obtained using an omni-directional antenna. This way, the gain in electric field strength due to beamforming can be quantified for the user. This 'beamforming gain' is evaluated in both LOS and NLOS conditions. Additionally, the spatio-temporal aspect of beamforming is explored through the exposure levels of the user and several static non-users.

**TABLE 2. Summary of scenarios. The different scenarios and their respective investigated parameters or effects are presented.**

| Scenario | Investigated parameters or effects |
|---|---|
| Single user | 1) Quantify beamforming gain<br>2) Investigate LOS and NLOS conditions<br>3) Assess spatio-temporal characteristics of exposure by evaluating exposure of static non-users |
| Two users | 1) Investigate the influence of adding the second user<br>2) Compare MRT and ZF precoding<br>3) Check the formation of wanted and unwanted hotspots<br>4) Assess influence of antenna array configuration on field strengths and SNR/SINR |
| Multiple users | 1) Investigate spatio-temporal coupling in a realistic environment<br>2) Determine the influence of increasing number of users on exposure<br>3) Determine the influence of precoding schemes<br>4) Determine difference in user/non-user exposure<br>5) Compare numerical results to ICNIRP limit |

Second, an additional user is introduced into the initial scenario (*two users* scenario in Table 2), with both users being served by the same BS site. The complete scenario is shown in Fig. 2. The two users follow distinct, strategically designed routes that ensure varying degrees of separation. This allows for scenarios where they are either closely spaced or significantly distant from one another. The SNR and electric field strengths of $4 \times 4$ and $8 \times 8$ antenna arrays are evaluated. MRT and ZF precoding schemes are compared under both LOS and NLOS conditions.

Finally, the scenario domain is expanded and is now served by two BS sites (*multiple users* scenario in Table 2). The impact of the number of active users on the exposure is assessed. The scenario initially includes 50 non-users with 10 active users. Users are progressively added in increments of 10, culminating in 50 users and 50 non-users. This results in five distinct cases, each with the same set of non-users, while varying the number of active users. As mentioned in Section II-B, scenario-specific variability is averaged out

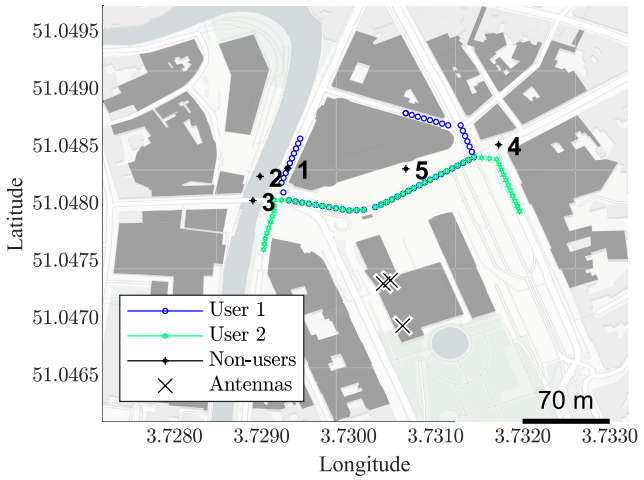


**FIGURE 2.** User routes with static non-users, corresponding to the *single user* (only user 1) and *two users* scenarios. The scenario is served by one BS site with three antennas (denoted by a black cross) covering different areas. The discrete points along the user routes are denoted by a blue circle (user 1) and a green diamond (user 2). Five static non-users (denoted by a black asterisk) are randomly placed in the environment. The environment is located in Ghent, Belgium.

**TABLE 3.** Beamforming gain, defined as the increase in electric field strength due to beamforming, for the user in the *single user* scenario. The user electric field strengths for a 5G antenna array with precoding are compared to an isotropic antenna. The beamforming gain (in dB) is calculated for both 4 × 4 and 8 × 8 antenna arrays. The averages over time are presented for LOS and NLOS positions of the user.

| | Beamforming gain [dB] | |
|---|---|---|
| Antenna array | LOS | NLOS |
| $4 \times 4$ | 16.8 | 20.7 |
| $8 \times 8$ | 23.5 | 26.8 |

by performing multiple simulations on the UGent HPC infrastructure. Each scenario is repeated ten times with newly generated agents within the same environment.

## III. RESULTS

### A. SINGLE USER

#### 1) BEAMFORMING GAIN

Table 3 presents the average beamforming gain for LOS and NLOS conditions, comparing $4 \times 4$ and $8 \times 8$ antenna array configurations. The beamforming gain is calculated from the electric field strength for the MaMIMO compared to an isotropic antenna. This comparison is done on a power dB scale: $20 \log_{10}(\frac{E_{\text{MaMIMO}}}{E_{\text{iso}}})$. The results indicate a 3 dB to 4 dB increase in beamforming gain between LOS and NLOS scenarios. Furthermore, the $8 \times 8$ configuration exhibits a 6 dB to 7 dB higher beamforming gain compared to the $4 \times 4$ configuration in both LOS and NLOS conditions. This outcome aligns with theoretical expectations, as the received signal strength scales with the number of antenna elements $N$ [3]. Consequently, the electric field strength should scale proportionally to $\sqrt{N}$, leading to a 6 dB difference between the $4 \times 4$ and $8 \times 8$ arrays. These observations

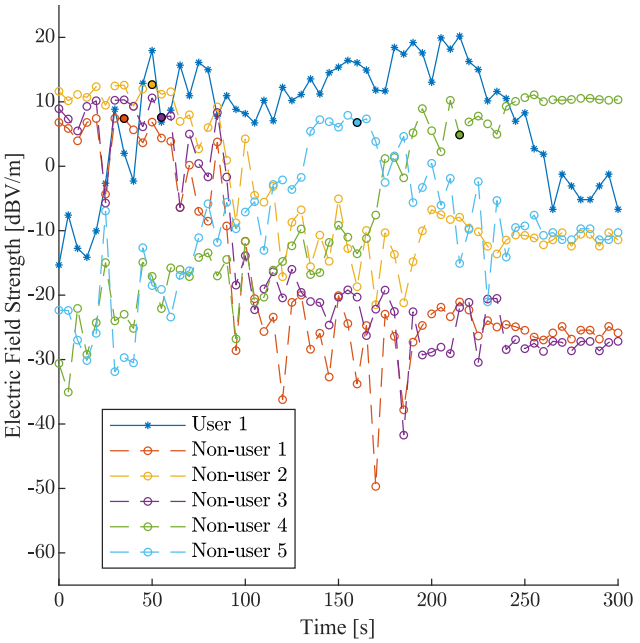


**FIGURE 3.** Spatio-temporal analysis. Temporal variation of electric field strengths for the user (denoted by blue asterisks) and five stationary non-users (denoted by circles with different colours). For each non-user, the time step where the user is closest is filled in and encircled in black. The antenna configuration is an 8 × 8 antenna array. The field strengths are presented in dB $\text{Vm}^{-1}$, calculated on a power dB scale relative to 1 $\text{Vm}^{-1}$. The LOS and NLOS regions of the user route are indicated. The specific variations in field strength as the user approaches a non-user shows that the spatial and temporal components of exposure are coupled.

are corroborated by results in [35], which show a linear relationship between the electric field strength and the increasing number of active antenna elements $N$. However, in that study, the transmit power was allowed to scale with $N$. In contrast, our analysis assumes a constant maximum transmit power, resulting in a field strength that scales as $\sqrt{N}$.

#### 2) SPATIO-TEMPORAL ANALYSIS

Fig. 3 illustrates the temporal variation of electric field strengths experienced by the user and the stationary non-users. The electric field strength is presented on a power dB scale relative to 1 $\text{V m}^{-1}$ (dB $\text{V m}^{-1}$). In this scenario, the transmitter employs an $8 \times 8$ antenna array. As the user transitions between LOS and NLOS conditions, the electric field strength variates approximately 20 dB. Non-users 1, 2, and 3 initially experience electric field strengths around 10 dB $\text{V m}^{-1}$ during the early time steps. This is due to their positioning within the primary beam direction, which targets the user under NLOS conditions. However, as the user moves further away, the field strengths for non-users 1 and 3 diminish to approximately $-25$ dB $\text{V m}^{-1}$ from 50 s to 100 s. For non-user 2, the strength decreases to around $-10$ dB $\text{V m}^{-1}$.

A similar trend is observed for non-user 5, whose field strength increases by 20 dB $\text{V m}^{-1}$ as the user approaches, particularly between 100 s and 200 s. Non-user4 exhibits a

$20\,\mathrm{dB\,V\,m^{-1}}$ increase in field strength towards the end of the user's trajectory, stabilizing at around $10\,\mathrm{dB\,V\,m^{-1}}$ once the user moves behind a building. This stabilization is attributed to non-user 4 being aligned with the main beam direction during this phase of the user's movement.

The significance of the relative positions of users and non-users in field strength is also documented in literature. For instance, in [35], LOS measurements demonstrate that a user or bystander aligned with the main beam direction could experience up to nine times higher (19 dB) exposure compared to those located outside the beam's path. Similarly, in [36], simulations confirm that employing directive antennas in 5G systems concentrates field levels at the user's location, thereby reducing average exposure across the wider environment. These studies illustrate the concept of beam steering towards users. However, it is important to note that the beamforming techniques utilized in these studies differ from the MRT precoding method applied in our analysis.

### B. TWO USERS

#### 1) INFLUENCE OF SECOND USER

Fig. 4a presents the SNR for user 1 as a function of time, highlighting the impact of introducing a second user into the scenario (as shown in Fig. 2). The results are presented for both $4 \times 4$ and $8 \times 8$ antenna arrays. When the second user is introduced, a reduction of approximately 3 dB in SNR is observed for user 1. This reduction is attributed to the division of transmit power between the two users when they are served by two separate beams. Similar observations are found in measurements [37]. The observed difference in SNR between the $4 \times 4$ and $8 \times 8$ configurations remains consistent with expectations, showing an approximate 6 dB difference due to the increased number of antenna elements $N$.

Fig. 4b shows the electric field strength for user 1 under the same conditions. The results confirm that the $\sqrt{N}$ dependence of the electric field strength with respect to the number of antenna elements holds. However, the introduction of a second user does not consistently result in either higher or lower field strengths. This discrepancy arises because SNR is a result of the desired signal for the target user, while the total electric field strength also includes contributions from interfering signals transmitted to the second user. Consequently, constructive interference can lead to an increase in field strength, as observed at around 100 s, while destructive interference may cause a decrease in field strength, as seen around 150 s.

#### 2) PRECODING SCHEMES

Fig. 5 presents heatmaps for MRT and ZF precoding schemes, using an $8 \times 8$ antenna array configuration. Fig. 5b and 5a correspond to MRT precoding, while Fig. 5d and 5c correspond to ZF precoding. When the users are positioned at a larger distance apart (59 m), the interference between them is minimal, resulting in similar heatmaps for MRT (5a) and ZF (5c). In this scenario, two distinct beams are formed:

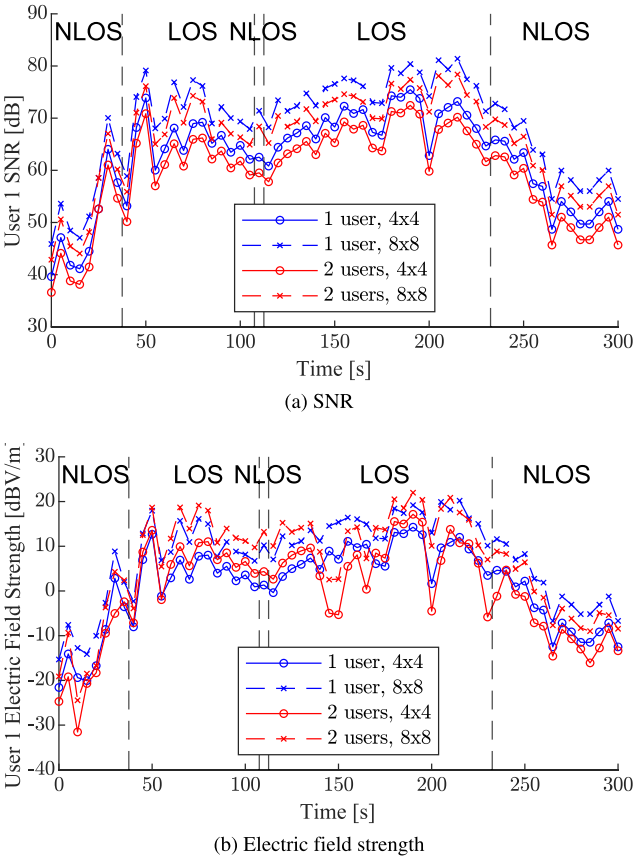


(a) SNR

(b) Electric field strength

**FIGURE 4. Comparison of SNR and electric field strength for user 1 between the *single user* and *two users* scenarios. The SNR (a) and electric field strength (b) for user 1 are presented as a function of time for different antenna array configurations. The LOS and NLOS regions of the user route are indicated.**

one directed towards the user in LOS and the other towards the buildings behind the user in NLOS. In general, the formed beams are relatively broad. Consequently, the ability of precoding to effectively reduce non-user exposure is suboptimal under these conditions.

When the inter-user distance decreases to 8 m, ZF precoding mitigates interference by selecting distinct transmission paths for each user. This leads to a difference in the heatmap between ZF (5d) and MRT (5b) precoding. Under MRT, a single broad beam is formed towards both users. For ZF precoding, unwanted hotspots emerge. The electric field strengths experienced by both users are approximately 9.6 dB lower with ZF, due to effective interference mitigation. While ZF reduces user exposure, the occurrence of the unwanted hotspots could limit the effectiveness of ZF in reducing non-user exposure.

### C. MULTIPLE USERS

#### 1) MRT PRECODING

Table 4 lists the median electric field strengths and interquartile ranges (IQRs) for the various scenarios involving different antenna array configurations and precoding schemes.

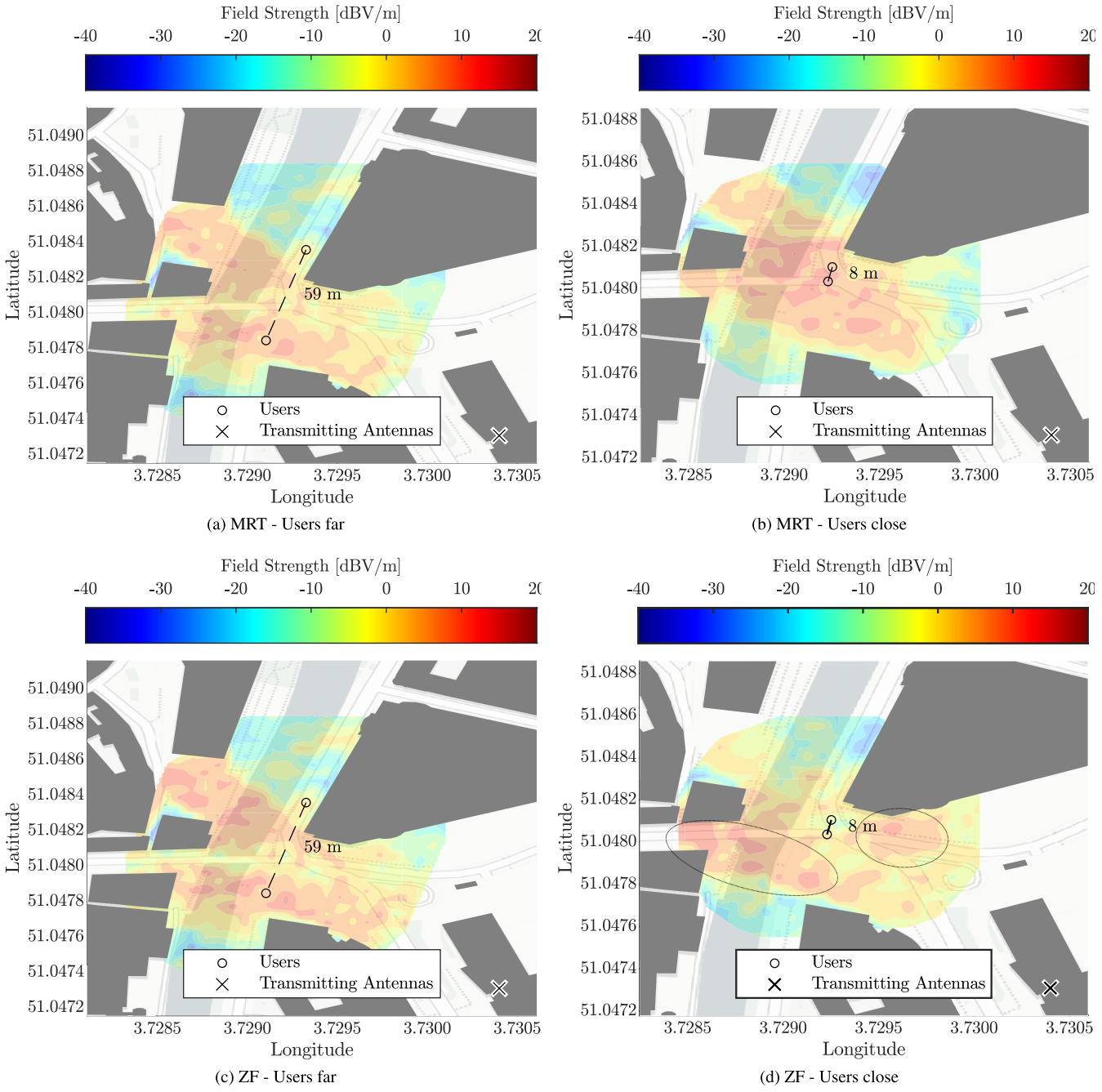


**FIGURE 5.** Heatmaps for the *two users* scenario. (a), (b) show the heatmaps for MRT precoding when the users (positions indicated by ∘) are 59 m apart (a) and 8 m apart (b). As the users move closer, the two beams cannot be separated anymore, and a single beam is created. (c), (d) illustrate the heatmaps for ZF precoding for the same setups. Similar heatmaps are observed between MRT (a) and ZF (c) when the users are distant from each other. While ZF precoding attempts to mitigate interference when users are close (d), unwanted hotspots are created (encircled on the figure).

A general decline in user field strength is observed with increasing user count. This is expected, as the power constraint in (6) splits the total transmitter for each antenna over its served users. The results further indicate that for MRT precoding, this decline in user field strengths with increasing numbers of users is dependent on the antenna array configuration. Specifically, as the number of users rises from 10 to 50, the median field strength decreases by 0.5 dB for a $4 \times 4$ antenna array and by 2.0 dB for an $8 \times 8$ antenna array. These findings indicate that larger antenna arrays experience a more pronounced reduction in individual user field strength as user count increases. This phenomenon can be attributed to the more uniform exposure distribution characteristic of smaller antenna arrays, even at lower user counts. In contrast, as the number of users grows, the exposure distribution of larger antenna arrays

**TABLE 4. Summary of electric field strength results over all the *multiple users* scenario. The median electric field strength (and interquartile range) for users and non-users are presented for across the different scenario configurations with 50 non-users.**

| | | Median Electric Field Strength (and IQR) [V/m] | | | |
|---|---|---|---|---|---|
| Number of users | Antenna array | MRT | | ZF | |
| | | Users | Non-users | Users | Non-users |
| 10 | $4 \times 4$ | 0.92 (1.30) | 0.61 (1.00) | 0.39 (0.71) | 0.38 (0.58) |
| | $8 \times 8$ | 1.68 (2.25) | 0.73 (1.39) | 1.04 (1.59) | 0.62 (1.05) |
| 20 | $4 \times 4$ | 0.92 (1.26) | 0.70 (1.05) | 0.24 (0.44) | 0.28 (0.41) |
| | $8 \times 8$ | 1.56 (2.00) | 0.89 (1.51) | 0.66 (1.15) | 0.53 (0.81) |
| 30 | $4 \times 4$ | 0.89 (1.21) | 0.72 (1.07) | 0.14 (0.30) | 0.18 (0.29) |
| | $8 \times 8$ | 1.42 (1.88) | 0.93 (1.51) | 0.48 (0.82) | 0.43 (0.63) |
| 40 | $4 \times 4$ | 0.87 (1.19) | 0.74 (1.07) | 0.09 (0.22) | 0.13 (0.22) |
| | $8 \times 8$ | 1.37 (1.84) | 0.99 (1.56) | 0.38 (0.68) | 0.38 (0.56) |
| 50 | $4 \times 4$ | 0.87 (1.19) | 0.77 (1.11) | 0.06 (0.15) | 0.09 (0.16) |
| | $8 \times 8$ | 1.33 (1.79) | 1.01 (1.58) | 0.31 (0.55) | 0.35 (0.50) |

progressively becomes more uniform, leading to a greater decrease in individual user field strengths. Despite this larger reduction with user count, the field strengths are consistently higher for the $8 \times 8$ configuration. For 10 users, the field strength difference between the two configurations is 5.2 dB, while for 50 users, it decreases to 3.7 dB. This deviation from the expected $\sqrt{N}$ dependence, as outlined in Section III-A, indicates a diminished impact of the antenna array size as the user count rises.

The IQRs for user field strengths also exhibit a reduction of 0.8 dB and 2.0 dB for the $4 \times 4$ and $8 \times 8$ configurations, respectively, as the user count increases from 10 to 50. Similar to the median values, the IQRs are higher for $8 \times 8$ configurations, with average differences of 4.8 dB and 3.5 dB observed for 10 and 50 users, respectively. This indicates that users with high SNR benefit more from the enhanced beamforming capabilities of the $8 \times 8$ array than users with lower SNR, causing greater variability in exposure levels. In addition, the results also show that users with higher exposure are impacted more by increasing users count than users with lower exposure.

For non-users, Table 4 shows that the decline in field strengths is less sensitive to the antenna configuration than for users. However, the exposure values remain generally higher for larger antenna arrays. As the number of users increases from 10 to 50, the median field strengths for non-users increase by 2.0 dB for the $4 \times 4$ array and 2.8 dB for the $8 \times 8$ array. The field strength difference between the two configurations is 1.6 dB for 10 users and increases to 2.4 dB for 50 users. For an $8 \times 8$ antenna, one would expect a lower median field strength for non-users, since the beams are more directional towards the user positions. However, the results suggest that, with an ABM based on population density and random user selection, non-user field strengths are also higher for an $8 \times 8$ array compared to a $4 \times 4$ array. This can be attributed to the fact that the users are stochatisically close to users. Therefore, the non-user field strengths are also higher for the $8 \times 8$ array.

The IQRs for non-users decrease by 0.9 dB and 1.1 dB for the $4 \times 4$ and $8 \times 8$ configurations, respectively, as the number of users increases from 10 to 50. However, the IQRs are consistently higher for the $8 \times 8$ configuration, with average differences of 2.9 dB and 3.1 dB for 10 and 50 users, respectively. These findings highlight that the user count influences non-user field strengths more than the number of antenna elements do. In addition, the number of antenna elements has a more substantial impact on user field strengths than on non-user field strengths.

The impact of user count and antenna array configurations on antenna performance and field strength is well-documented in the literature. For instance, the authors in [12] demonstrate that increasing the number of antenna elements significantly enhances the absolute antenna gain. Specifically for MRT, they report a gain increase of 3.5 dB when the number of antenna elements is increased from 16 to 64 for a fixed set of 10 users, which is comparable to our observed increase of 5.2 dB in field strength between the $8 \times 8$ and $4 \times 4$ arrays. Furthermore, they also highlight that as the number of active users increases, the overall antenna gain tends to diminish due to a broader distribution of beamforming patterns. They report a reduction of 2.4 dB in gain as the number of users increases from 1 to 10. This trend is consistent with our findings, where a decrease of 2.0 dB is observed between 10 and 50 users. However, while the precoding implementation in [12] is similar to the one adopted in this study, their simulation focuses on a single BS, and the maximum time-averaged antenna gain does not map directly to the resulting field strength distribution.

The influence of user count is also confirmed by measurements in [38], which shows that higher user densities lead to more dispersed beam patterns. In addition, increasing the number of active users also increases the chance of an increase in transmitting antennas, which will generally increase the non-user field strengths. This effect is confirmed in [39] and [40].

### 2) COMPARISON WITH ZF PRECODING

Table 4 demonstrates that, compared to MRT precoding, the application of ZF precoding results in generally lower field strengths for both users and non-users. Contrary to expectations, the potential formation of unintended hotspots associated with ZF precoding do not increase average

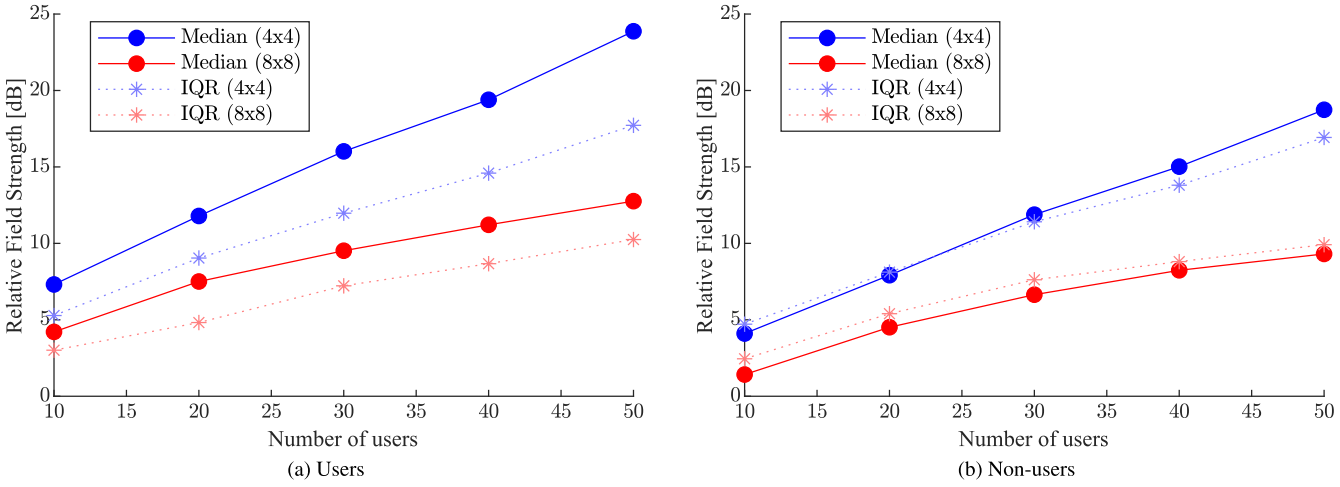


**FIGURE 6.** MRT-ZF comparison for the *multiple users* scenarios. Relative median field strength and IQR over all scenario configurations and over time between MRT and ZF precoding as function of user count. The quantities are presented on power dB scale, calculated as $20\log_{10}(\frac{E_{\text{MRT}}}{E_{\text{ZF}}})$. Results for different antenna arrays are provided for both users (a) and non-users (b).

exposure for non-users. This outcome may be attributed to the use of an ABM that incorporates population density, potentially leading to non-users stochastically being located in proximity to users. Consequently, non-user exposure levels decrease under ZF precoding.

For users, ZF precoding reduces the median field strength by as much as $0.83\,\text{V}\,\text{m}^{-1}$ compared to MRT precoding in a $4 \times 4$ configuration with 10 users. This demonstrates the effectiveness of ZF in mitigating interference and reducing user exposure. This trend is consistent across all configurations and varying user densities, underscoring the capacity of ZF to minimize exposure through enhanced interference suppression. Although the reductions in field strength for non-users are comparatively smaller, they remain statistically significant. In the $8 \times 8$ configuration, non-user field strengths decrease by $0.11\,\text{V}\,\text{m}^{-1}$ for 10 users and $0.16\,\text{V}\,\text{m}^{-1}$ for 50 users when switching from MRT to ZF.

These results indicate that while ZF primarily targets user-side interference reduction, it also achieves a moderate reduction in non-user exposure. Notably, non-user exposure decreases with increasing user count, in contrast to the MRT case where non-user exposure rises with the number of users. This observation reinforces the hypothesis that the spatial distribution of non-users, influenced by population density, leads to their positioning near users, thereby reducing exposure due to increased interference mitigation for larger user counts.

Fig. 6 presents the relative differences in median field strengths and interquartile ranges (IQRs) between MRT and ZF precoding across varying user densities for two antenna array configurations. These relative field strengths are presented on a power dB scale: $20\log_{10}(\frac{E_{\text{MRT}}}{E_{\text{ZF}}})$. The results reveal a more pronounced disparity between the two precoding schemes for the $4 \times 4$ array compared to the $8 \times 8$ array, which can be attributed to the limited interference mitigation capacity of the $4 \times 4$ array. Specifically, with an increasing number of users, the difference between MRT and ZF field strengths becomes more significant, reaching an increase of 15 dB for the $4 \times 4$ array in contrast to a 5 dB increase for the $8 \times 8$ array. This aligns with the enhanced spatial multiplexing capabilities of the $8 \times 8$ array, which allows for more effective management of interference among closely positioned users.

The increasing divergence with higher user counts suggests that ZF precoding will reduce exposure more as user count rises, likely due to the growing complexity of spatial multiplexing multiple users. For non-users, the relative median field strengths are, on average, 5 dB and 3 dB lower than for users in the $4 \times 4$ and $8 \times 8$ configurations, respectively. This finding is consistent with the observation that interference suppression techniques primarily benefit users. Despite the stochastic reduction in exposure levels achieved by ZF compared to MRT, non-users positioned in unintended hotspots partially counteract this reduction, leading to smaller differences in field strengths between the two schemes for non-users.

In the literature, the authors in [12] show that ZF results in lower normalized antenna gains than MRT. This will ultimately result in lower observed field strengths overall, which corresponds with our results. In addition, in [41], it is indicated that eigen-mode zero-forcing results in a bigger reduction in exposure than eigen-beamforming as the user count increases. These two beamforming techniques operate similarly to ZF and MRT respectively. Specifically, the differences in observed field strengths for the two methods found in this study are 0 dB for a single user, 0.2 dB for two users, 1.2 dB for five users, and 3.1 dB for eight users. This trend closely corresponds to the trend depicted in Fig.6.

Moreover, the similarity in relative IQRs for both users and non-users indicates that the overall impact of the

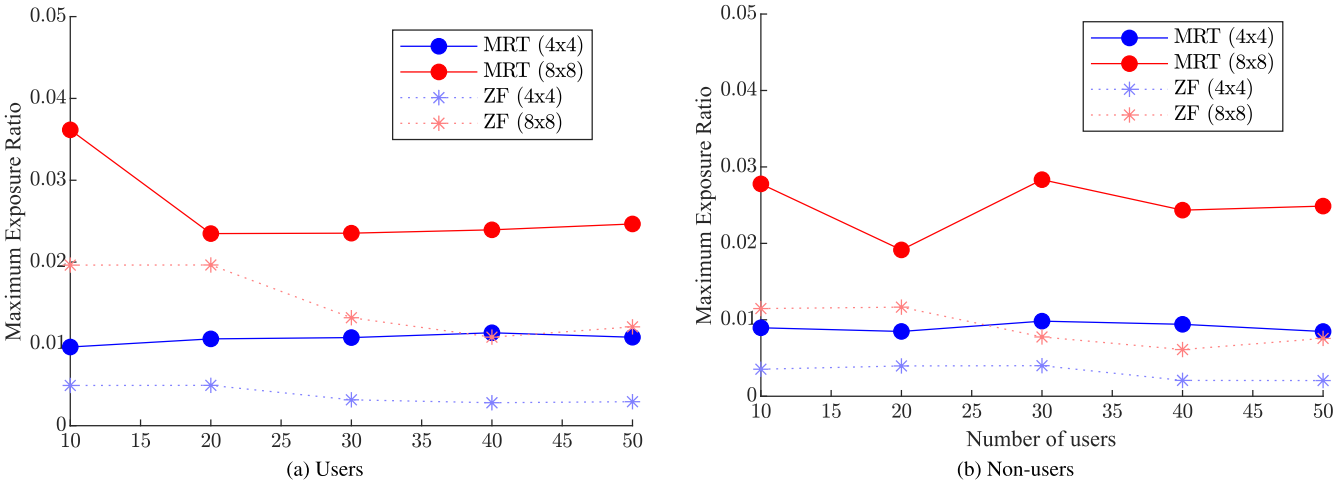


**FIGURE 7.** Maximum exposure evaluation. The maximum exposure ratio $\xi$ (see (16)) for users (a) and non-users (b) as function of number of users. The highest observed exposure is below 4% of the ICNIRP reference value. Higher maximum exposures are observed for the $8 \times 8$ array compared to the $4 \times 4$ array. For MRT, there is no correlation between user count and maximum exposure. For ZF, the maximum exposure decreases with user count.

chosen precoding scheme on variability in exposure remains comparable for both groups. This suggests that while ZF precoding effectively reduces median exposure levels compared to MRT, its impact on the distribution of exposure across the population is the same for both users and non-users.

### 3) MAXIMUM EXPOSURE

Fig. 7 presents the maximum exposure values across all iterations of each scenario, expressed as a ratio relative to the ICNIRP exposure guidelines (as outlined in Section II-C). These values represent the theoretical worst-case scenario for a specific number of users within the study area. However, because the total transmit powers of the antennas are used irrespective of the number of users being served, these maximum values may not correspond to a realistic worst-case scenario in operational conditions [42]. Nevertheless, they still offer valuable insights into the potential maximum exposure levels under high BS power conditions.

The results demonstrate that maximum exposure levels across all configurations remain well below the ICNIRP guidelines for the general public, ensuring that maximum exposures comply with established health guidelines. The maximum exposure ratio is less than 4 % over all scenarios and configurations.

For the MRT precoding scheme, maximum exposure levels exhibit no significant correlation with the number of active users. This outcome likely arises from the calculation of maximum values across multiple iterations, where absolute maxima are determined by the specific spatial arrangements in each iteration. In certain scenarios, a cluster of users may lead to elevated exposure levels due to interference, despite the distribution of transmit power among a larger user base.

In contrast, the maximum exposure levels for ZF precoding display a decreasing trend with increasing user numbers. This trend can be attributed to the interference mitigation capabilities of ZF precoding, which reduce the occurrence of scenario-specific exposure peaks resulting from overlapping beams. By minimizing interference among an increasing number of users, ZF effectively lowers the maximum exposure values. However, a minor exception occurs between 40 and 50 users, where a slight increase of 0.01 % is observed in the maximum non-user exposure. This likely results from a specific scenario in which the addition of the 10 users increase the magnitude of an unintended hotspot at the location of the non-user.

## IV. CONCLUSION

In this study, a spatio-temporal method, denoted as the "ABM-RT method", is proposed to assess human exposure to electromagnetic fields (EMFs) in 5G networks in realistic urban environments. The method integrates an agent-based model (ABM) for pedestrian movement simulation and a Ray-Tracing (RT) approach to calculate electric field strengths for both active users and non-users. Various antenna configurations and precoding schemes, specifically maximum ratio transmission (MRT) and zero-forcing (ZF), are analyzed to understand their impact on user and non-user exposure.

The results demonstrate that an $8 \times 8$ antenna array results in 5.2 dB to 3.7 dB higher field strengths compared to an $4 \times 4$ array, depending on the number of active users. In addition, non-user exposure also increases with larger antenna arrays, with differences of up to 2.4 dB. Comparing precoding schemes, ZF precoding is found to reduce user and non-user exposure compared to MRT by up to 9.6 dB and 1.1 dB respectively. The analysis of interquartile ranges (IQRs) further suggests that the impact of precoding scheme on the exposure distributions is effectively the same for users and non-users. Moreover, the analysis of maximum exposure levels relative to the ICNIRP limit show that even in the worst-case scenarios, the maximum observed exposure

remains well below 4 % of the ICNIRP reference level for the general public.

These findings underline the need for spatio-temporal assessment of exposure in 5G networks. The stochastic results also provide valuable insights for network designers and policymakers to optimize network configurations and mitigate EMF exposure risks.

Future research will explore the impact of different pedestrian movement patterns and varying beamwidth configurations on EMF exposure. Additionally, the method can be extended to evaluate exposure in different environments. The exposure levels in different countries, cities and environment types will be quantified and categorized. Lastly, the model could be adapted to include next-generation networks such as 6G with higher frequencies or different antenna technologies like distributed MaMIMO.

## ACKNOWLEDGMENT

Views and opinions expressed are however those of the authors only and do not necessarily reflect those of the European Union or the Health and Digital Executive Agency. Neither the European Union nor the granting authority can be held responsible for them.

## REFERENCES

[1] Ericsson. (2024). *Mobile Data Traffic Forecast—Mobility Report*. Accessed: May 2024. [Online]. Available: https://www.ericsson.com/en/reports-and-papers/mobility-report/dataforecasts/mobile-traffic-forecast

[2] E. Björnson, J. Hoydis, and L. Sanguinetti, "Massive MIMO networks: Spectral, energy, and hardware efficiency," *Found. Trends Signal Process.*, vol. 11, nos. 3–4, pp. 154–655, 2017.

[3] T. L. Marzetta, E. G. Larsson, and H. Yang, *Fundamentals of Massive MIMO*. Cambridge, U.K.: Cambridge Univ. Press, 2016.

[4] International Commission on Non-Ionizing Radiation Protection (ICNIRP), "Guidelines for limiting exposure to electromagnetic fields (100 khz to 300 ghz)," *Health Phys.*, vol. 118, pp. 483–524, May 2020.

[5] M. Röösli and D. Vienneau, "Epidemiological exposure assessment," in *Epidemiology of Electromagnetic Fields*. Boca Raton, FL, USA: CRC Press, 2014, pp. 35–55.

[6] M. Matalatala Tamasala, S. Shikhantsov, M. Deruyck, E. Tanghe, D. Plets, S. K. Goudos, L. Martens, and W. Joseph, "Combined ray-Tracing/FDTD and network planner methods for the design of massive MIMO networks," *IEEE Access*, vol. 8, pp. 206371–206387, 2020.

[7] M. Deruyck, W. Joseph, E. Tanghe, and L. Martens, "Reducing the power consumption in LTE-advanced wireless access networks by a capacity based deployment tool," *Radio Sci.*, vol. 49, no. 9, pp. 777–787, Sep. 2014.

[8] H. C. Nguyen, G. R. MacCartney, T. Thomas, T. S. Rappaport, B. Vejlgaard, and P. Mogensen, "Evaluation of empirical ray-tracing model for an urban outdoor scenario at 73 GHz E-band," in *Proc. IEEE 80th Veh. Technol. Conf. (VTC-Fall)*, Vancouver, BC, Canada, Sep. 2014, pp. 1–6.

[9] M. Z. Aslam, Y. Corre, E. Björnson, and E. G. Larsson, "Large-scale massive MIMO network evaluation using ray-based deterministic simulations," in *Proc. IEEE 29th Annu. Int. Symp. Pers., Indoor Mobile Radio Commun. (PIMRC)*, Bologna, Italy, Sep. 2018, pp. 1–5.

[10] S. Shikhantsov, A. Thielens, G. Vermeeren, E. Tanghe, P. Demeester, L. Martens, G. Torfs, and W. Joseph, "Hybrid ray-Tracing/FDTD method for human exposure evaluation of a massive MIMO technology in an industrial indoor environment," *IEEE Access*, vol. 7, pp. 21020–21031, 2019.

[11] S. Shikhantsov, A. Guevara, A. Thielens, G. Vermeeren, P. Demeester, L. Martens, G. Torfs, S. Pollin, and W. Joseph, "Spatial correlation in indoor massive MIMO: Measurements and ray tracing," *IEEE Antennas Wireless Propag. Lett.*, vol. 20, pp. 903–907, 2021.

[12] S. Shikhantsov, A. Thielens, S. Aerts, L. Verloock, G. Torfs, L. Martens, P. Demeester, and W. Joseph, "Ray-Tracing-Based numerical assessment of the spatiotemporal duty cycle of 5G massive MIMO in an outdoor urban environment," *Appl. Sci.*, vol. 10, no. 21, p. 7631, Oct. 2020.

[13] N. Noé and F. Gaudaire, "Numerical modeling of downlink electromagnetic wave exposure generated by 5G beamforming antennas," *Comp. Rendus. Phys.*, vol. 22, no. S1, pp. 15–24, Jun. 2021.

[14] M. Celaya-Echarri, L. Azpilicueta, J. Karpowicz, V. Ramos, P. Lopez-Iturri, and F. Falcone, "From 2G to 5G spatial modeling of personal RF-EMF exposure within urban public trams," *IEEE Access*, vol. 8, pp. 100930–100947, 2020.

[15] D. E. Egea-Lopez, D. M. Mallik, D. L. Clavier, and D. P. Gaillot, "Generation of electromagnetic exposure maps for 5G communications," in *Proc. 18th Eur. Conf. Antennas Propag. (EuCAP)*, 2024, pp. 1–4.

[16] M. Mallik, A. A. Tesfay, B. Allaert, R. Kassi, E. Egea-Lopez, J.-M. M.-G.-Pardo, J. Wiart, D. P. Gaillot, and L. Clavier, "Towards outdoor electromagnetic field exposure mapping generation using conditional GANs," *Sensors*, vol. 22, no. 24, p. 9643, Dec. 2022.

[17] UUSG. Surv. (Oct. 2024). *EarthExplorer*. Accessed: Oct. 15, 2024. [Online]. Available: https://earthexplorer.usgs.gov/

[18] *BuildingMaterialPermittivity—MATLAB & Simulink—MathWorks*. Accessed: May 22, 2024. [Online]. Available: https://nl.mathworks.com/help/comm/ref/buildingmaterialpermittivity.html

[19] *OpenStreetMap*. Accessed: Oct. 2023. [Online]. Available: https://www.openstreetmap.org/

[20] *Simple3DBuildingsV1—OpenStreetMap Wiki*. Accessed: May 22, 2024. [Online]. Available: https://wiki.openstreetmap.org/wiki/Simple3DBuildingsV1

[21] "Effects of building materials and structures on radio wave propagation above 100 MHz," P Series Radio Wave Propag. P.2040, Recommendation ITU-R, 2015, vol. 1.

[22] A. W. Mbugua, Y. Chen, L. Raschkowski, L. Thiele, S. Jaeckel, and W. Fan, "Review on ray tracing channel simulation accuracy in Sub-6 GHz outdoor deployment scenarios," *IEEE Open J. Antennas Propag.*, vol. 2, pp. 22–37, 2021.

[23] *Kaart Zendantennes | Departement Omgeving—vlaamse*. Accessed: May 2024. [Online]. Available: https://omgeving.vlaanderen.be/nl/zoek-zendantennes-op-de-kaart

[24] *5G: Study on Channel Model for Frequencies From 0.5 To 100 GHz*, Standard TR38.901, 3rd Gener. Partnership Project (3GPP), 2017.

[25] S. Abar, G. K. Theodoropoulos, P. Lemarinier, and G. M. P. O'Hare, "Agent based modelling and simulation tools: A review of the state-of-art software," *Comput. Sci. Rev.*, vol. 24, pp. 13–33, May 2017.

[26] *Global Human Settlement—GHSL Homepage—European Commission*. Accessed: Mar. 2024. [Online]. Available: https://human-settlement.emergency.copernicus.eu

[27] Google for Developers. *Directions API Overview*. Accessed: May 2024. [Online]. Available: https://developers.google.com/maps/documentation/directions/overview

[28] *Ray Tracing for Wireless Communications—MATLAB & Simulink—MathWorks*. Accessed: Mar. 2024. [Online]. Available: https://nl.mathworks.com/help/comm/ug/ray-tracing-for-wireless-communications.html

[29] F. Aghaei, H. B. Eldeeb, L. Bariah, S. Muhaidat, and M. Uysal, "Comparative characterization of indoor VLC and MMW communications via ray tracing simulations," *IEEE Access*, vol. 11, pp. 90345–90357, 2023.

[30] G. E. Athanasiadou and A. R. Nix, "Investigation into the sensitivity of the power predictions of a microcellular ray tracing propagation model," *IEEE Trans. Veh. Technol.*, vol. 49, no. 4, pp. 1140–1151, Jul. 2000.

[31] *How to Normalize a Precoding Matrix? | Wireless Future Blog*. Accessed: Feb. 2024. [Online]. Available: https://ma-mimo.ellintech.se/2019/09/29/how-to-normalize-a-precoding-matrix

[32] H. Q. Ngo, *Massive MIMO: Fundamentals and System Design*. Linkping, Sweden: Linkping University, 2015.

[33] E. Björnson and Ö. T. Demir, *Introduction To Multiple Antenna Communications and Reconfigurable Surfaces*. Boston, MA, USA: Now Publishers, 2024.

[34] E. Korkmaz, S. Aerts, R. Coesoij, C. R. Bhatt, M. Velghe, L. Colussi, D. Land, N. Petroulakis, M. Spirito, and J. Bolte, "A comprehensive review of 5G NR RF-EMF exposure assessment technologies: Fundamentals, advancements, challenges, niches, and implications," *Environ. Res.*, vol. 260, Nov. 2024, Art. no. 119524.

[35] F. Héliot, T. H. Loh, D. Cheadle, Y. Gui, and M. Dieudonne, "An empirical study of the stochastic nature of electromagnetic field exposure in massive MIMO systems," *IEEE Access*, vol. 10, pp. 63100–63112, 2022.

[36] M. Gargiulo, A. Iodice, D. Riccio, and G. Ruello, "Electromagnetic propagation software tool for planning and analyzing 5G networks," in *Proc. IEEE 6th Int. Forum Res. Technol. Soc. Ind. (RTSI)*, Naples, Italy, Sep. 2021, pp. 424–428.

[37] K. Deprez, L. Verloock, L. Colussi, S. Aerts, M. Van den Bossche, J. Kamer, J. Bolte, L. Martens, D. Plets, and W. Joseph, "In-situ 5G NR base station exposure of the general public: Comparison of assessment methods," *Radiat. Protection Dosimetry*, vol. 198, no. 6, pp. 358–369, May 2022.
[38] P. Joshi, D. Colombi, B. Xu, C. Di Paola, J. E. Bischoff, S. S. Zhekov, and C. Törnevik, "Long-term network-based assessment of the actual output power of base stations in a 5G network," in *Proc. 18th Eur. Conf. Antennas Propag. (EuCAP)*, Glasgow, U.K., Mar. 2024, pp. 1–5.
[39] M. Matalatala, M. Deruyck, S. Shikhantsov, E. Tanghe, D. Plets, S. Goudos, K. E. Psannis, L. Martens, and W. Joseph, "Multi-objective optimization of massive MIMO 5G wireless networks towards power consumption, uplink and downlink exposure," *Appl. Sci.*, vol. 9, no. 22, p. 4974, Nov. 2019.
[40] M. A. Salem, H. S. Lim, M. Y. Chua, S. F. Chien, C. C. Zarakovitis, C. Y. Ng, and N. Z. A. Rahman, "Investigation of EMF exposure level for uplink and downlink of 5G network using ray tracing approach," *Int. J. Technol.*, vol. 13, no. 6, p. 1298, Nov. 2022.
[41] M. Rybakowski, K. Bechta, C. Grangeat, and P. Kabacik, "Impact of beamforming algorithms on the actual RF EMF exposure from massive MIMO base stations," *IEEE Access*, vol. 11, pp. 141956–141964, 2023.
[42] D. Colombi, P. Joshi, B. Xu, F. Ghasemifard, V. Narasaraju, and C. Törnevik, "Analysis of the actual power and EMF exposure from base stations in a commercial 5G network," *Appl. Sci.*, vol. 10, no. 15, p. 5280, Jul. 2020.

**MATTHIAS LEEMAN** received the M.Sc. degree in engineering physics from Ghent University, Ghent, Belgium, in 2024. He is currently pursuing a Ph.D. degree in engineering physics with imec and Ghent University. His research interests include assessment and mapping of human exposure to radio frequency electromagnetic (RF-EMF) fields in 5G and future generations of wireless access networks. He uses ray-tracing simulations and in-situ measurements in urban environments for geostatistical mapping of RF-EMF exposure.

**ROBIN WYDAEGHE** received the B.Sc. and M.Sc. degrees in engineering physics from Ghent University, Ghent, Belgium, in 2019 and 2021, respectively. He is currently pursuing a Ph.D. degree in engineering physics with imec and Ghent University. His research interests include computational electrodynamics, numerical assessment of human electromagnetic field exposure, and propagation modeling of next generation wireless networks.

**JEROEN VAN DER STRAETEN** received the M.Sc. degree in electrical engineering: electronic circuits and systems from Ghent University, Ghent, Belgium, in 2023, where he is currently pursuing a Ph.D. degree with the WAVES-IMEC Research Group, Department of Information technology, and imec. His research interests include the design of sensors to measure radio frequency electromagnetic (RF-EMF) exposure induced by 5G telecommunication for FR1 and FR2. He is also interested in automated RF-EMF measurement setups.

**SAMUEL GOEGEBEUR** received the M.Sc. degree in engineering physics from Ghent University, in 2022, where he is currently pursuing the Ph.D. degree in 5G spatio-temporal exposure modeling with the WAVES Group, Department of Information Technology. His research interests include raytracing simulations for geostatistical 5G exposure modeling and in-situ electromagnetic field exposure measurements campaigns.

**GÜNTER VERMEEREN** is currently a Postdoctoral Researcher with the WAVES Research Group, where he is involved in the research on of radio-frequency dosimetry, electromagnetic exposure, and on-body propagation. He is the author of 57 publications in international journals and of 54 papers on national and international scientific conferences. His research interests include numerical modeling (FDTD, MoM) as well as measurements of electromagnetic fields in the proximity of humans (exposure as well as on- and in-body propagation). Part of his research results are also included in the international standard IEC 62232. Since 2013, he has been involved in the research on medical imaging systems with a focus on the modeling of the electromagnetic fields in hybrid MRI systems.

**WOUT JOSEPH** (Senior Member, IEEE) was born in Ostend, Belgium, in October 1977. He received the M.Sc. degree in electrical engineering and the Ph.D. degree from Ghent University, Ghent, Belgium, in July 2000 and in March 2005, respectively. His Ph.D. work dealt with measuring and modeling of electromagnetic fields around base stations for mobile communications related to the health effects of the exposure to electromagnetic radiation. From 2007 to 2012, he was a Postdoctoral Fellow with the Research Foundation Flanders (FWO-V), Brussels, Belgium. Since October 2009, he has been a Professor of experimental characterization of wireless communication systems. He has been a PI with imec, Ghent, since 2017. His professional interests are electromagnetic field exposure assessment, propagation for wireless communication systems, antennas, and calibration. Furthermore, he specializes in wireless performance analysis and quality of experience.